We are IntechOpen,
the world's leading publisher of
Open Access books
Built by scientists, for scientists

4,800
Open access books available

122,000
International authors and editors

135M
Downloads

Our authors are among the

154
Countries delivered to

TOP 1%
most cited scientists

12.2%
Contributors from top 500 universities

BOOK CITATION INDEX
CLARIVATE ANALYTICS
INDEXED

WEB OF SCIENCE™

Selection of our books indexed in the Book Citation Index
in Web of Science™ Core Collection (BKCI)

Interested in publishing with us?
Contact book.department@intechopen.com

Numbers displayed above are based on latest data collected.
For more information visit www.intechopen.com

Failure Diagnosis of Squirrel-Cage Induction Motor with Broken Rotor Bars and End Rings

Takeo Ishikawa

Additional information is available at the end of the chapter

Abstract

This chapter investigates the diagnosis of not only broken bar but also broken end ring faults in an induction motor. The difference between the broken bars and broken end ring segments is experimentally clarified by the Fourier analysis of the stator current. This difference is verified by two-dimensional finite element (FE) analysis that takes into consideration the voltage equation and the end ring. The electromagnetic field in the undamaged motor and the motor with broken bars and broken end ring segments is analyzed. The effect of the number of broken bars and broken end ring segments on the motor performance is clarified. Moreover, transient response is analyzed by the wavelet analysis.

Keywords: Failure diagnosis, finite element method, motor current signature analysis, wavelet analysis

1. Introduction

Squirrel-cage induction motors are widely used in many industrial applications because they are cost effective and mechanically robust. However, production will stop if these motors fail. Therefore, early detection of motor faults is highly desirable. Induction motor faults are summarized in [1] and [2], and rotor failures account for approximately 10% of the total induction motor failures. Several studies have carried out diagnosis of induction machines using motor current signature analysis (MCSA). For example, Davio et al. proposed a method to diagnose rotor bar failures in induction machines based on the analysis of the stator current

during start-up using the discrete wavelet transform (DWT) [3]. Moreno et al. developed an automatic online diagnosis algorithm for broken-rotor-bar detection, which was optimized for single low-cost field-programmable gate array implementation [4]. Guasp et al. proposed a method based on the identification of characteristic patterns introduced by fault components in the wavelet signals obtained from the discrete wavelet transformation of transient stator currents [5]. Kia et al. proposed a time-scale method based on DWT to make the broken-bar fault diagnosis slip independent [6]. Gritli et al. carried out diagnosis of induction machines using DWT under a time-varying condition [7]. However, most of the literature has studied only broken-bar faults, and broken end ring faults have been marginally dealt with. For example, Bouzida et al. dealt with the fault diagnosis of induction machines with broken rotor bars and end ring segment and loss of stator phase during operation using DWT [8]. Concerning the FE analysis of rotor failures in induction motors, several papers have been presented. For example, Mohammed et al. studied the broken rotor bar and stator faults using FE and discrete wavelet analyses [9]. Weili et al. analyzed the flux distribution in the air gap of an induction motor with one and two broken rotor bars [10]. Faiz et al. analyzed the stator current under different numbers of broken bars and different loads of an induction motor [11]. They dealt with broken rotor bars but not a broken end ring.

This chapter addresses not only broken bar but also broken end ring faults. First, we manufacture some rotors with broken bars or end rings [12]. Next, the difference between the broken end ring segments and broken bars is verified by MCSA [12]. The electromagnetic field in the rotor is analyzed to clarify the effect of the number of broken bars and broken end ring segments on the motor performance [13]. Moreover, the stator voltage and current waveforms in a transient response are analyzed by the wavelet analysis.

2. Induction motor with broken rotor and experimental system

Figure 1 shows the photographs of a rotor with broken bars and a broken end ring segments that we have manufactured [13]. Figure 1(a) shows a rotor with one broken bar drilled at the center of the rotor, and Fig. 1(b) shows a rotor with two broken bars drilled at the adjacent aluminum bars. Figure 1(c) shows a rotor with a broken segment in the end ring, which is made by cutting aluminum. Figure 1(d) shows a rotor with two broken segments in the end ring, which are separated by two rotor bars. Figure 1(e) shows a rotor with two broken segments in the end ring whose distance is 45 degrees, that is, 90 electrical degrees. The experimental motor shown in Fig. 2 has the following specifications: 50 Hz, 200 V, 400 W, four poles, and 1,400 min^{-1} speed.

Figure 3 shows the experimental system for the failure diagnosis, which is composed of a 200-V 1.1-kVA 3-A inverter, an induction motor, a torque meter, and a servo motor used as load. Figure 4 shows the developed measurement system using NI cDAQ and Lab VIEW [14]. Lab VIEW is a system design platform and development environment for visual programming language and can be easily used for data acquisition in Microsoft Windows. Figure 4(a) shows the interface part, which is composed of a channel selector, x and y scales, trigger, and two
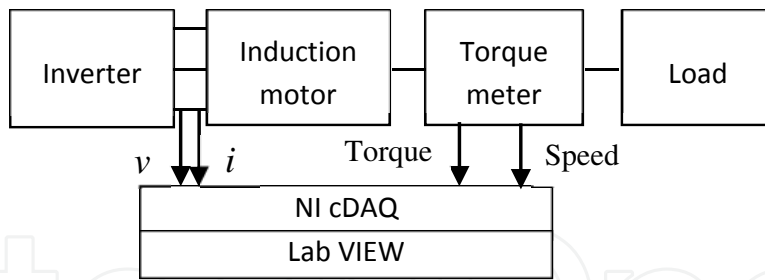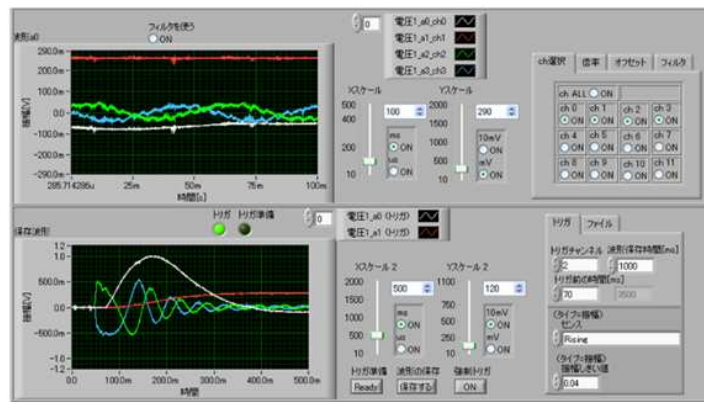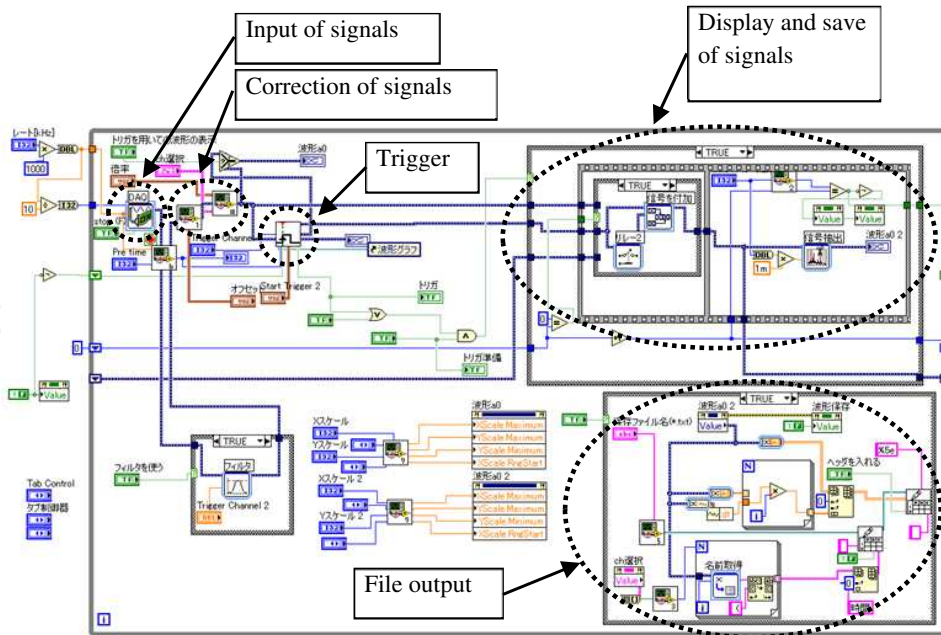
(a) One broken bar [1 bar]   (b) Two broken bars [2 bars]

(c) One broken segment   (d) Two broken segments   (e) Two broken segments (90)

[1 ring]   [2 rings]   [2 rings (2)]

Figure 1. Rotors with broken bars and end rings.

Figure 2. Experimental induction motor.

displays that look like a multi-channel oscilloscope. Figure 4(b) shows a Lab VIEW block, which is composed of blocks for the acquisition and correction of data, trigger detection, and saving of data. Several physical variables, including the stator voltage v, stator current i, torque, and speed are measured by the NI cDAQ and Lab VIEW and are then analyzed by Fourier analysis.

Figure 3. Experimental measurement system.

(a) Interface.

(b) Block diagram using Lab VIEW

Figure 4. Developed measurement system [14].

3. Fourier analysis of the measured data

Figure 5 shows the Fourier analysis of the stator current at a rated speed of 1,400 min^{-1}, where the Fourier component of several rotors is shown at every 0.33 Hz to easily compare the broken situations. Here, 1 bar, 2 bars, 1 ring, 2 rings, and 2 rings (2) mean one broken bar [see Fig. 1(a)], two adjacent broken bars [Fig. 1(b)], end ring broken at one position [Fig. 1(c)], end ring broken at two positions separated by two rotor bars [Fig. 1(d)], and end ring broken at two positions separated by five rotor bars, that is, 90 electrical degrees [Fig. 1(e)], respectively.

(a) Fourier analysis.

(b) Enlarged around 36.7 Hz,   (c) 43.3 Hz,   (d) 56.7 Hz,   (e) 63.3 Hz

Figure 5. Fourier analysis of the measured stator current at the rated speed.

In Fig. 3, the inverter rating is 1.1 kVA, which is a sufficient capacity for the 400-W experimental induction motor. Therefore, the Fourier analysis of the stator voltage did not include the (1 ± 2s)f Hz components, where s is the slip and f is the fundamental supply frequency. Because the servo motor is a synchronous motor with surface permanent magnets, the torque ripple is very small. Therefore, the effect of the inverter source and the load equipment on this measurement was very small. However, because the measured results are sensitive to the experimental setup, the experiment was performed three times. We expected a slight difference in the mechanical loss because the connection of the motor, the torque meter, and the servo motor could not be perfect even under the same situation. To take this slight difference into account,

the experimental system was set up for every measurement. Therefore, three sets of measured results were slightly different.

We found 50 ± 6.67 Hz components, that is, $(1 ± 2s)f$ Hz as expected [15]. Let us explain the frequency of $(1 ± 2s)f$ Hz. When the rotor is running at slip s and the supply frequency is f, the frequency of the forward current in the rotor is sf. If the rotor has a defect, such as a broken bar or broken end ring, a backward current frequency of $-sf$ can flow in the rotor. The forward current frequency sf in the rotor is considered as frequency f at the stator. Because the rotor is running at $(1 - s)f$, the frequency recognized at the stator is $sf + (1 - s)f = f$. In contrast, the backward current frequency of $-sf$ is considered as a stator frequency of $(1 - 2s)f$ because $-sf + (1 - s)f = (1 - 2s)f$. Then, a torque with a frequency of $2sf$ is developed because the stator current has two frequencies f and $(1 - 2s)f$. The torque produces a vibration of $2sf$, and thus, the rotor speed becomes $(1 - s)f ± 2sf$. This speed vibration and the forward current produce a stator current frequency of $(1 - s)f ± 2sf + sf = (1 ± 2s)f$.
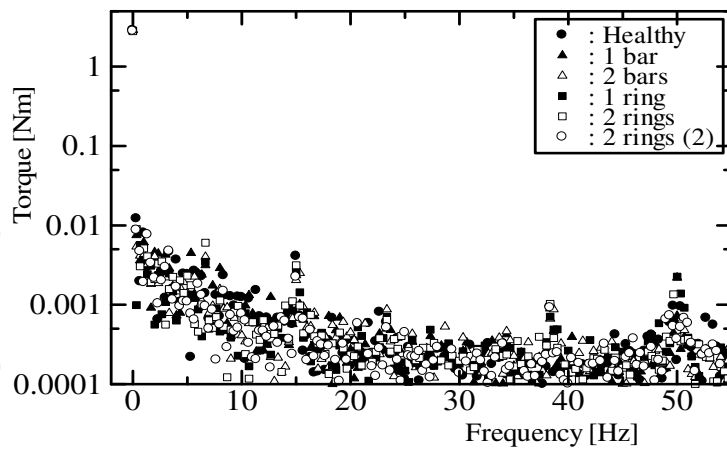
In each fault, the components at 50 - 6.67 Hz, that is, $(1 - 2s)f$ Hz, are approximately the same as those at 50 + 6.67 Hz, that is, $(1 + 2s)f$ Hz. Table 1 shows the average components at $(1 ± 2s)f$ Hz. The order of the components for the different faults is as follows: [2 rings] > [1 ring] > [2 bars] > [1 bar] > [2 rings (2)] > [healthy]. Therefore, we have experimentally clarified that we can detect the fault of the rotor end ring segments and rotor bars from the $(1 ± 2s)f$ Hz component of the stator current at the rated speed. In contrast, it is difficult to detect the failure type from the Fourier analysis of the stator current at $(1 ± 2s)f$ Hz because no order of the components relative to the failure type is available.

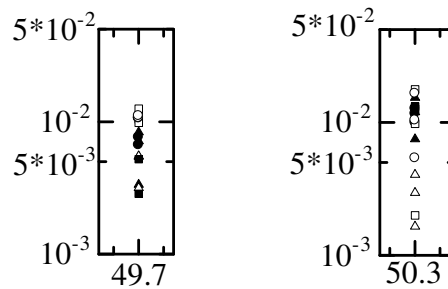|	43.33 Hz	50 Hz	56.67 Hz
Healthy	0.0010 A	2.818 A	0.0009 A
1 bar	0.0135 A	2.755 A	0.0119 A
2 bars	0.0176 A	2.890 A	0.0193 A
1 ring	0.0286 A	2.872 A	0.0258 A
2 rings	0.0306 A	2.725 A	0.0333 A
2 rings (2)	0.0076 A	2.760 A	0.0072 A

Table 1. Fourier components of the measured stator current.

Figure 6 shows the Fourier analysis of the stator current under a no-load condition. The rotating speed of 1,495 min^{-1} was almost the same. We also find 50 ± 0.33 Hz components, that is, $(1 ± 2s)f$ Hz components. However, because no order of the components relative to the failure types is available, it is difficult to detect the failure type by Fourier analysis of the stator current under the no-load condition.

Figure 7 shows the Fourier analysis of the torque at the rated speed of 1,400 min^{-1}. We find 6.67 Hz components, that is, $2sf$ Hz. The order of the components for the $2sf$ for different faults was not clear. For the end ring fault, the order of the components is as follows: [2 rings] > [1 ring]

(a) Fourier analysis

(b) Enlarged around 49.7 Hz   (b) Enlarged around 50.3 Hz

Figure 6. Fourier analysis of the measured stator current at no load.

> [2 rings (2)]. However, the component of [2 rings (2)] is approximately the same as that of the healthy motor. For the bar fault, the component of [2 bars] was approximately the same as that of [1 bar]. Therefore, it is difficult to detect the difference in the faults of the rotor end rings and rotor bars by Fourier analysis of the torque even at the rated speed.

4. Simulation of induction motor with broken rotor bars and broken end ring segments

4.1. Analysis method

The experimental motor has rotor skew of one slot pitch. Although a three-dimensional FE analysis is necessary to consider the rotor skew, it is very time consuming. This study calculates the electromagnetic field in the motor using a two-dimensional FE method, which considers the voltage equation and the rotor end ring. The cross section of the motor is shown in Fig. 8. The stator has 36 slots, and the rotor has 44 slots. The following assumptions have been made:

1.   Two-dimensional analysis is employed, and the skew in the rotor is ignored.

(a) Fourier analysis

Enlarged around (b) 6.67 Hz for the end ring and (c) 6.67 Hz for the bar.

Figure 7. Fourier analysis of the measured torque at the rated speed.

2. Rotor bars and end ring are insulated from the rotor core, and no current flows from the rotor bars to the rotor core.

3. The rotating speed is constant.
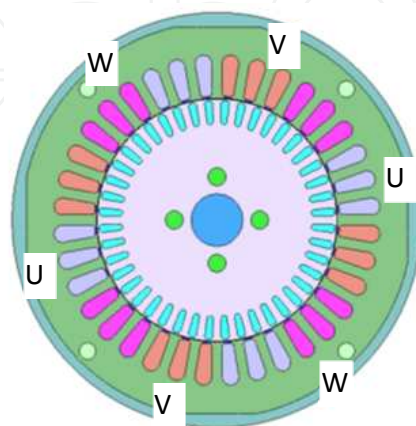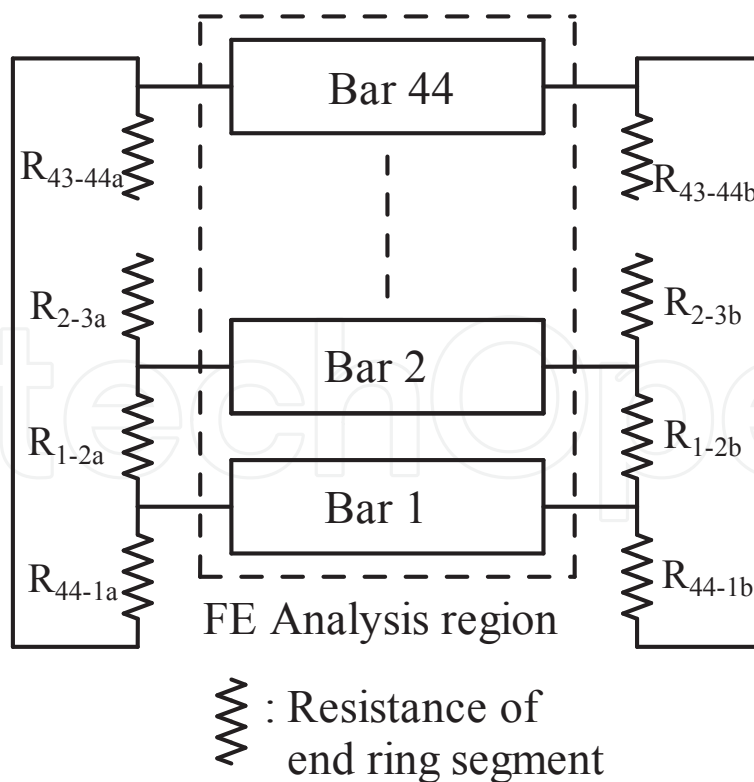
4. The supply voltage is assumed to be sinusoidal.

Figure 8. Cross section of the experimental induction motor.

Although the motor is fed by a pulse width modulation (PWM) inverter, the Fourier components of the measured stator current around the switching frequency differ very slightly among the rotor fault types. Therefore, the PWM inverter does not affect the harmonic components of the stator current.

Figure 9 shows the FE analysis region and the connection of the end ring segments in the rotor where 44 bars are included in the FE analysis. Because the end ring is connected to each rotor bar, it is represented by 44 conductor segments whose resistance is R. For example, R_{1-2a} represents the resistance of the end ring segment between bars 1 and 2, and its value is expressed by

$$R = \rho \frac{l}{S} \tag{1}$$

where of aluminum is. l is the length of conductor segment in the circumferential direction, and S is the area of cross section. Fins connected to the end ring for cooling are neglected. When rotor bar 1 is broken, its conductivity is set to zero. When part of the end ring is broken between bars 1 and 2, resistance R_{1-2a} is set to infinity. The FE analysis was conducted for 3 s with 6,750 steps, where the number of nodes and elements were 34,909 and 60,866, respectively.

Figure 9. FE analysis region and end ring segments.

4.2. Analysis results

Figure 10 shows the Fourier analysis of the calculated stator current at the rated speed of 1,400 min^{-1}. We find the $(1 \pm 2s)f$ and $(1 \pm 4s)f$ components. Table 2 shows the calculated results of the Fourier analysis at the fundamental and $(1 \pm 2s)f$ components. By comparing these results with those in Table 1, we find that the calculated fundamental components are slightly smaller than the measured ones, and the calculated $(1 \pm 2s)f$ components are larger than the measured ones. We believe that these differences are attributed to the assumption where the skew is not taken into account in the calculation. We also verify from the calculated results that the $(1 \pm 2s)f$ components of the end ring faults are larger than those of the bar faults and that the $(1 \pm 2s)f$ component of the end ring broken at two positions separated by electrical radian is smaller than that of the other faults.
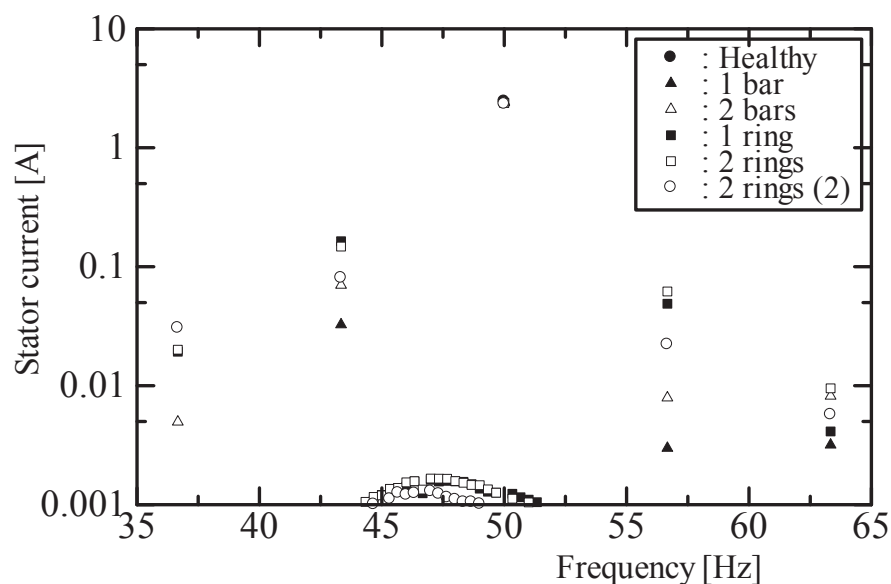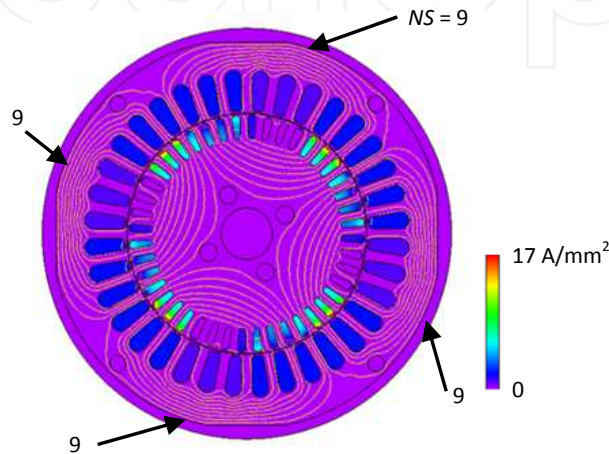

Figure 10. Fourier analysis of the calculated stator current.

	43.33 Hz	50 Hz	56.67 Hz
Healthy	0.0002 A	2.455 A	0.0003 A
1 bar	0.0326 A	2.434 A	0.0030 A
2 bars	0.0701 A	2.411 A	0.0079 A
1 ring	0.1637 A	2.390 A	0.0488 A
2 rings	0.1477 A	2.374 A	0.0618 A
2 rings (2)	0.0807 A	2.335 A	0.0222 A

Table 2. Fourier components of the measured stator current.

4.3. Electromagnetic field in the motor calculated by FEM

An example of the magnetic flux and eddy current distribution in the healthy motor under the rated speed with rated-load condition is shown in Fig. 11. Because this motor is a four-pole machine, the magnetic flux distribution is periodic in every one-fourth region, that is, in every nine stator slots. Here, we denote the number of stator slots in the same group of magnetic flux lines as *NS*. Then, the *NS* for each pole is 9, 9, 9, and 9, and there is no distortion in the magnetic flux distribution.

Figure 11. Distribution of the magnetic flux and eddy current in the healthy motor.

Figure 12 shows the distribution of the magnetic flux and eddy current in the motor with two broken bars under different rotor positions, namely, that where the magnetic flux does not pass through the broken bars [Fig. 12(a)] and that where it passes through the broken bars [Fig. 12(b)]. In Fig. 12(a), the eddy current distribution in the rotor bars is approximately the same as that in the healthy motor shown in Fig. 11, and the *NS* under each pole is approximately 8.5, 9.5, 8.5, and 9.5, indicating that magnetic flux distortion occurs. On the other hand, Fig. 12(b) shows a rotor bar where the eddy current density is very high, and the *NS* for each pole is approximately 9, 9, 10, and 8. These magnetic distortions, shown in Figs. 12 (a) and (b), are repeated.

Figure 13 shows the distribution of the magnetic flux and eddy current in the motor with a broken end ring segment under different rotor positions. No rotor bar exhibits a very high eddy current density, and the number of stator slots included in the flux lines for each pole is different. The *NS* for each pole is approximately 8.5, 9, 9, and 9.5 in Fig. 13(a) and approximately 8, 8.5, 10, and 9.5 in Fig. 12(b). These magnetic flux distortions are repeated. As explained in Chapter 3, these magnetic distortions produce a stator current frequency of $(1 \pm 2s)f$.

4.4. Effect of the number of broken bars and end ring segments

Next, we discuss the effect of the number of broken bars and broken end ring segments on the motor performance. Figure 14 shows the Fourier components of the stator current and torque
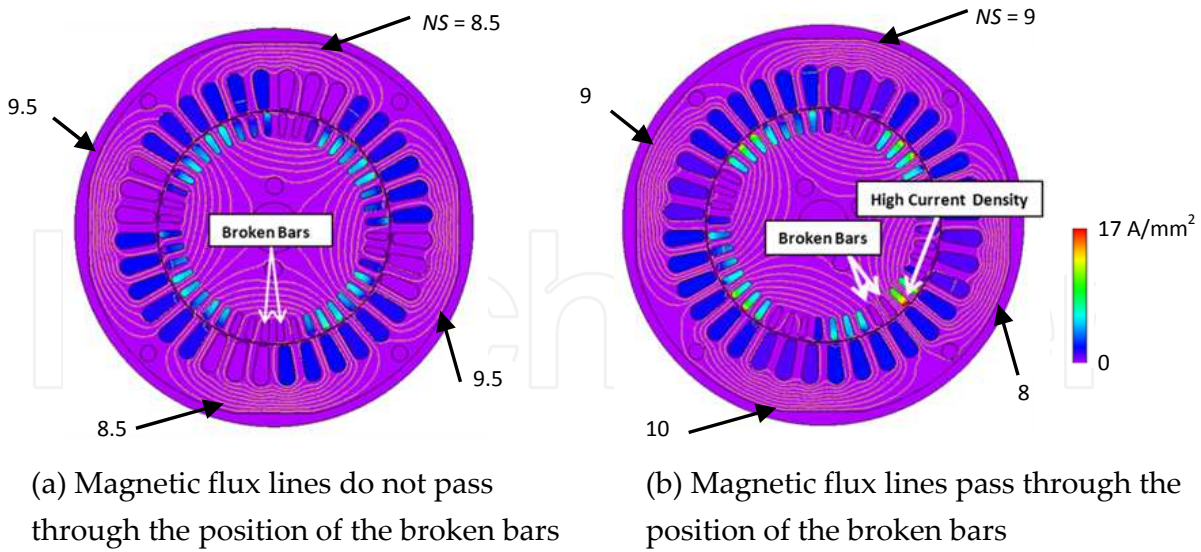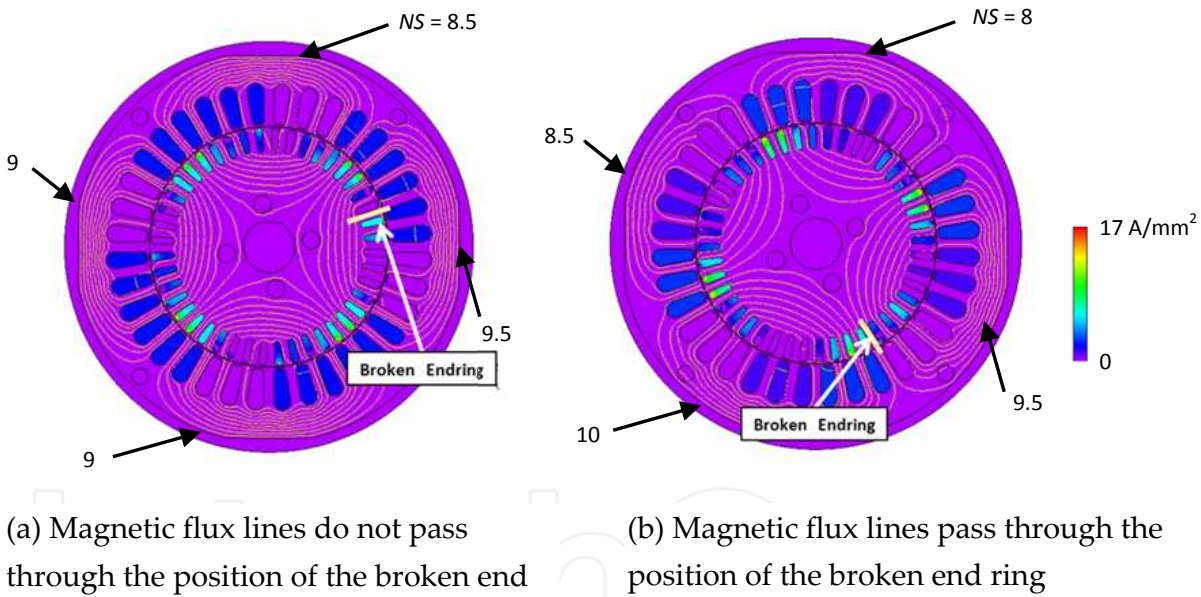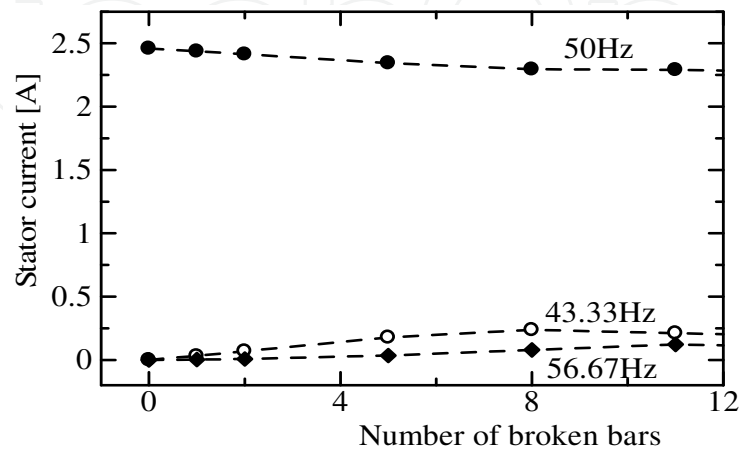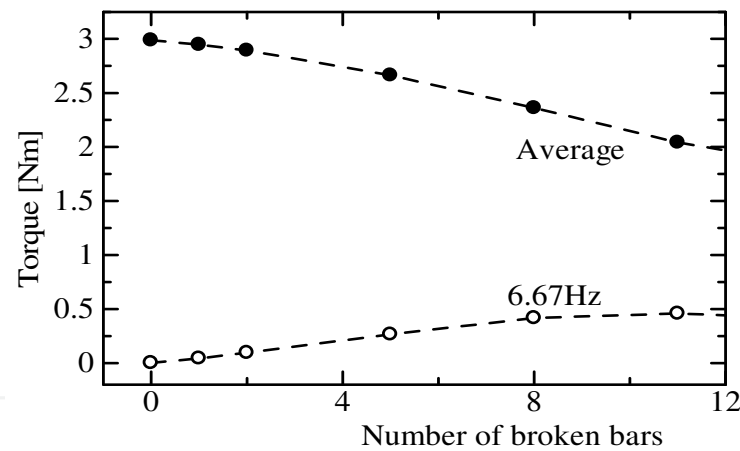
(a) Magnetic flux lines do not pass
through the position of the broken bars

(b) Magnetic flux lines pass through the
position of the broken bars

Figure 12. Distribution of the magnetic flux and eddy current in the motor with two broken bars under different rotor positions.

(a) Magnetic flux lines do not pass
through the position of the broken end

(b) Magnetic flux lines pass through the
position of the broken end ring

Figure 13. Distribution of the magnetic flux and eddy current in the motor with a broken end ring segment under different rotor positions.

for different numbers of broken bars. The fundamental components of the stator current and the average torque decrease, and the $(1 \pm 2s)f$ component of the stator current and the $2sf$ component of the torque increase when the number of broken bars increases. Figure 15 shows the Fourier components of the stator current and torque for different numbers of end ring segments. The fundamental components of the stator current and the average torque also decrease, and the $(1 \pm 2s)f$ component of the stator current and $2sf$ component of the torque approximately increase when the number of broken end ring segments increases. Tables 1 and

2 show that when the number of faults is small, the components for the different faults appear in the following order: [2 rings] > [1 ring] > [2 bars] > [1 bar] > [2 rings (2)] > [healthy]. In contrast, the comparison of Figs. 14 and 15 shows that the $(1 \pm 2s)f$ component of the stator current for the broken bars is larger than that for the broken end ring when the number of faults is greater than three.
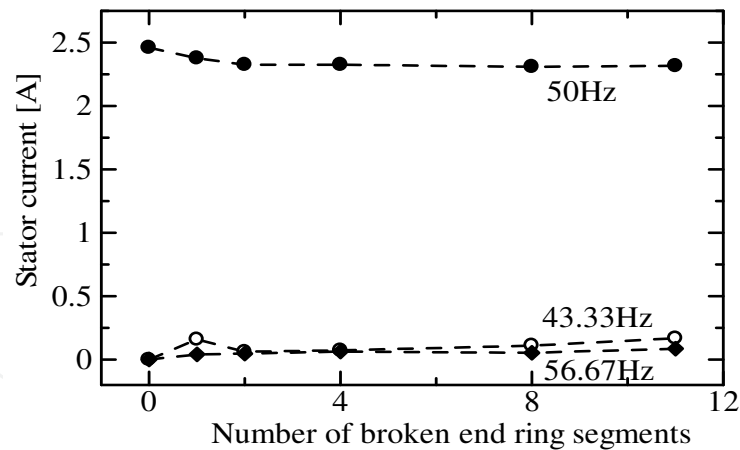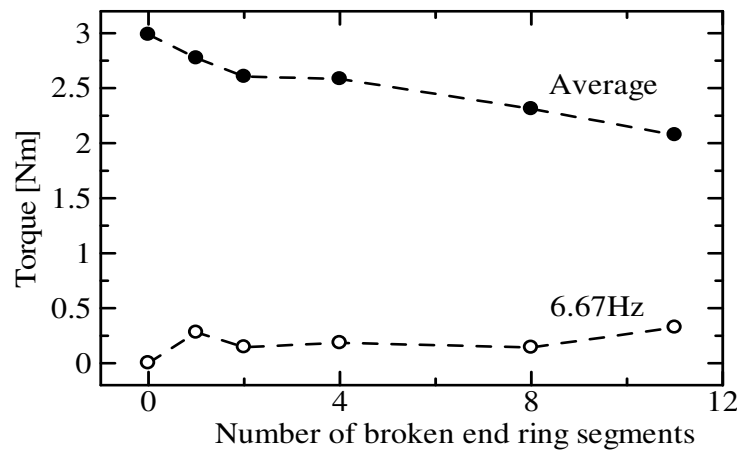

(a) Stator current

(b) Torque

Figure 14. Stator current and torque for different numbers of broken bars.

5. Wavelet analysis

We have discussed about the failure diagnosis of broken end ring segments and broken bars in induction motor at the steady state using the Fourier analysis. In this section, the transient performance of an inverter-fed induction motor is discussed by using the wavelet analysis. There are two kinds of wavelet transform; continuous and discrete ones.

(a) Stator current

(b) Torque

Figure 15. Stator current and torque for different numbers of broken end ring segments.

5.1. Continuous wavelet analysis

Let us make a brief introduction of continuous wavelet transform. Figure 16 shows the waveform of a signal and its wavelet analysis, which shows equipotential lines in the frequency and time plane. Although there are several kinds of Wavelet function – Morlet, Paul, and Derivative of Gaussian – Fig. 16 is the result of using the Morlet function, where the number of waves is 30. We can find high value region around 100 Hz and from 0.3 to 0.6 s and around 400 Hz and from 0.4 to 0.7 s.

We investigate transient response of an inverter-fed induction motor, where the control strategy is an open loop and the motor has no-load. The step responses of the stator voltage, stator current, and motor speed were measured when a start signal was input to the inverter. Figures 17 and 18 show the Wavelet analysis of the stator current i_u and stator voltage V_{uv} using the Morlet function, where the number of waves is two, for the healthy motor and for the motor with two broken bars. We can find a very slight difference in the Wavelet analysis of the stator
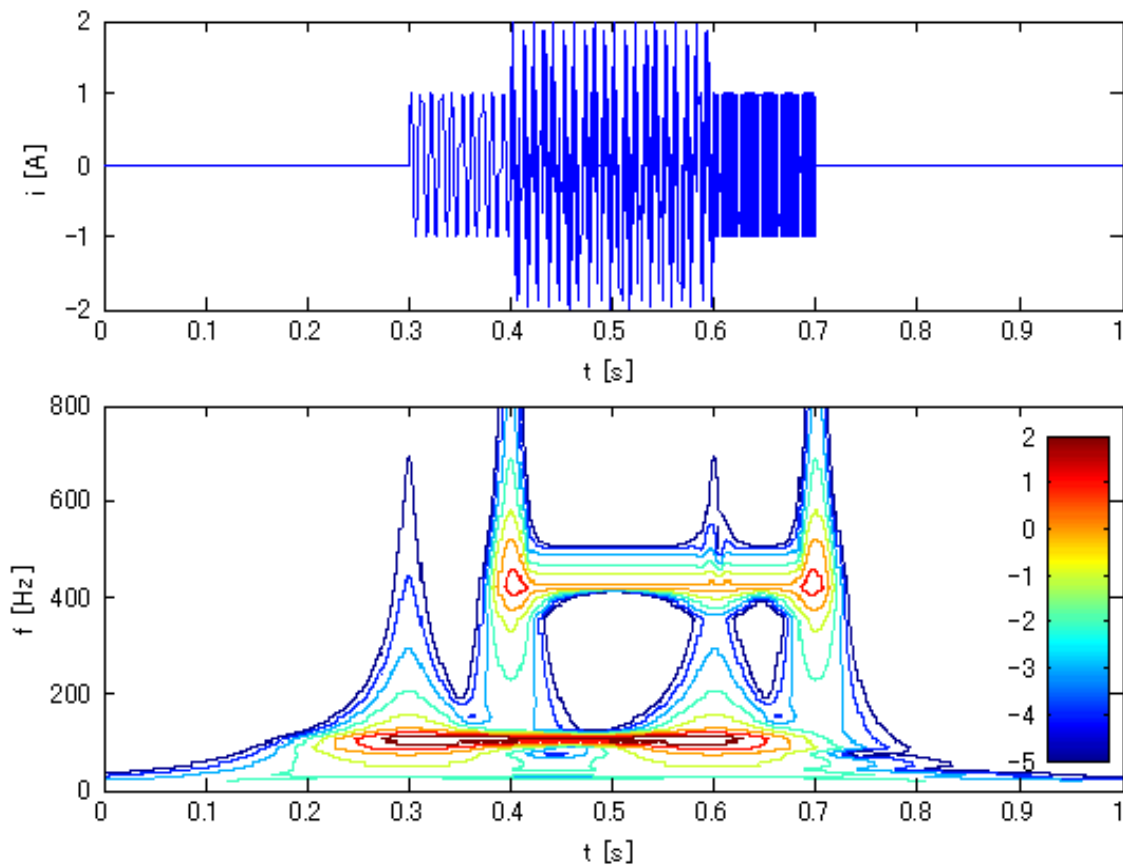
Figure 16. An example of the continuous wavelet analysis using the Morlet mother function.
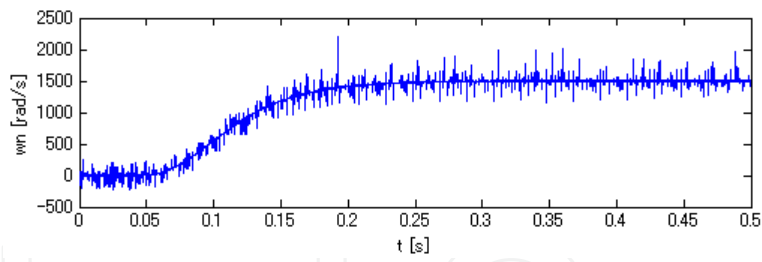
current between the healthy rotor and two broken bars. There are large components at high frequency before the motor starts, namely, time is from 0 to 0.05 s. As discussed before, the rotor fault produces the components of $(1 \pm 2s)f$. The component becomes 150 Hz when the rotor is stopping, that is, $s = 1$. It is shown that there is no difference in the stator voltage. Therefore, it is difficult to distinguish the rotor defect by using the continuous wavelet transform of the stator current in the starting operation with no-load condition.

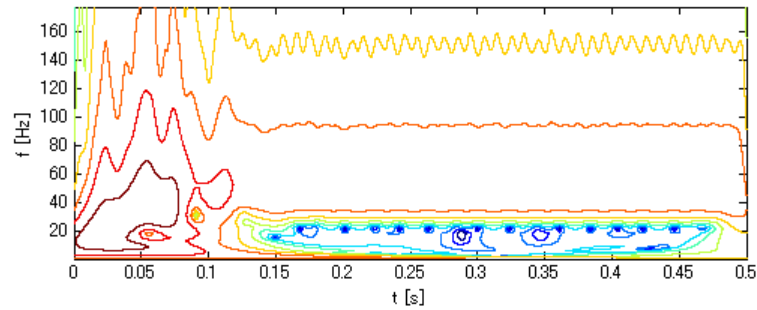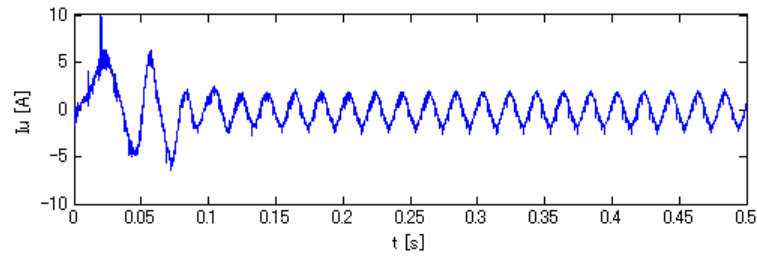## 5.2. Discrete wavelet analysis

The discrete wavelet transform of a signal is calculated by passing it through a series of filters. As it is well known, the use of wavelet signals, that is, approximation and high-order details, resulting from discrete wavelet transform constitutes an interesting advantage because these signals act as filters. Moreover, the computational time of discrete wavelet transform is much shorter than that of continuous wavelet transform. Figure 19 shows the discrete wavelet analysis for the same signal as shown in Fig. 16. It is found that the component of 100 Hz appears in d6 and signal of 450 Hz component appears in d4 detail.

Table 3 shows frequency bands by decomposition in multi-levels. Figures 20 and 21 show discrete wavelet signals of stator current i_u of the motor with the healthy rotor and two broken bars. It is shown that there are large components of d7 at $t = 0.05$ s, and a large component of
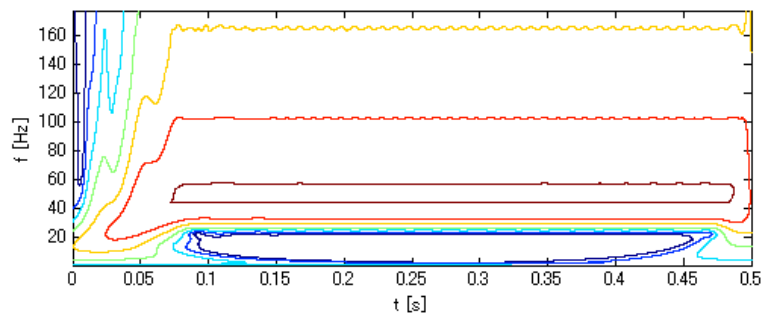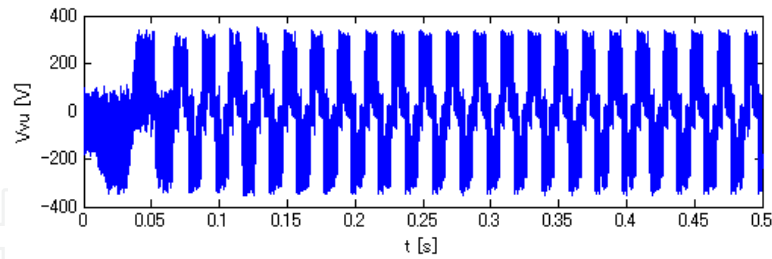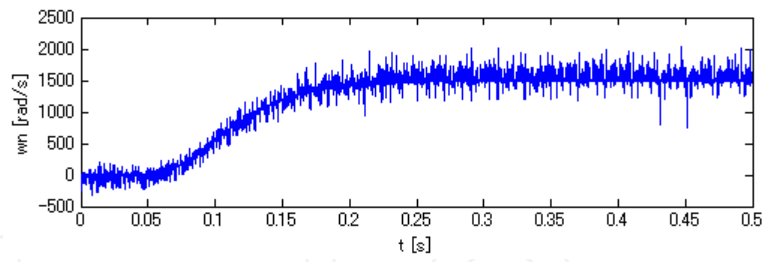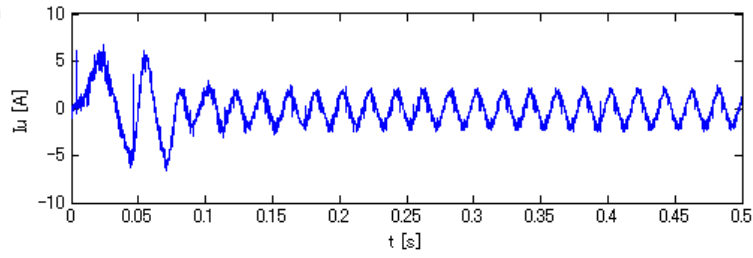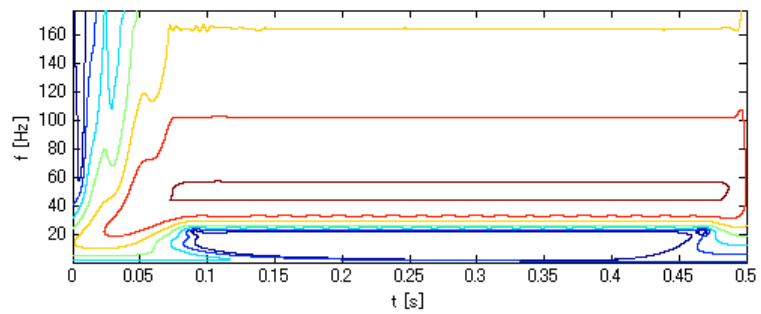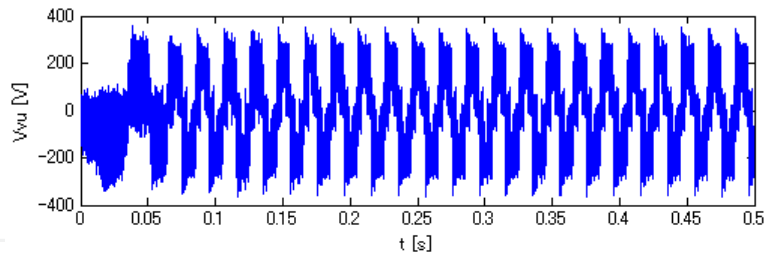
(a) Speed response.

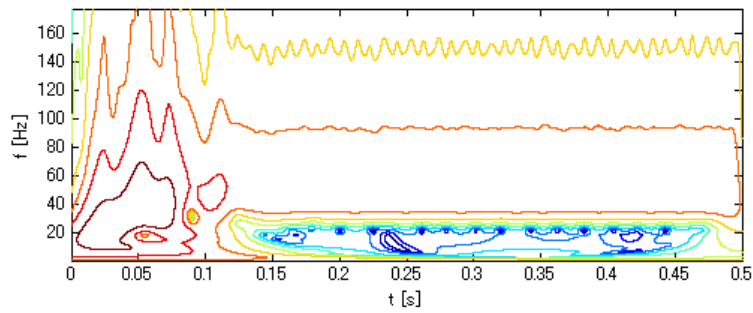(b) Stator current.

(c) Stator voltage.

Figure 17. Continuous wavelet analysis of healthy rotor.

(a) Speed response.

(b) Stator current.

(c) Stator voltage.

Figure 18. Continuous wavelet analysis of the motor with two broken bars.
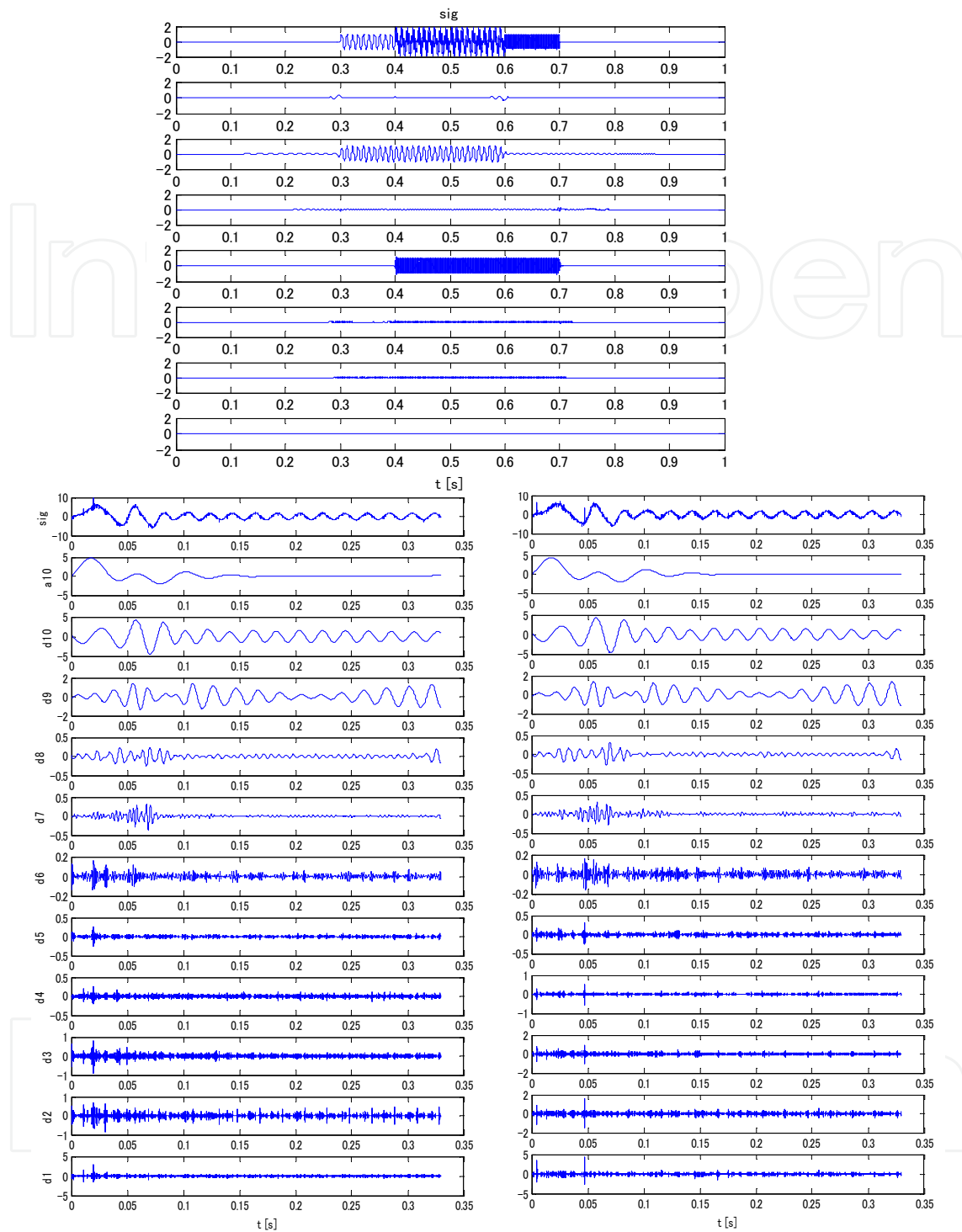
Figure 19. An example of the discrete wavelet analysis.

d8 at $t = 0.07$ s and a large component of d9 at $t = 0.12$ s. These components correspond to the frequency of $(1 + 2s)f$ Hz. We can find a slight difference of the components in these frequency bands between the healthy rotor and the rotor with two broken bars, especially in d2 through d6 details from 0 to 0.1 s.

Approximation and details	Frequency bands [Hz]
a10	0 – 24
d10	24 – 49
d9	49 – 98
d8	98 – 195
d7	195 – 391
d6	391 – 781
d5	781 – 1,563
d4	1,563 – 3,125
d3	3,125 – 6,250
d2	6,250 – 12,500
d1	12,500 – 25,000

Table 3. Frequency bands by decomposition in multi-levels.

6. Conclusions

This study has analyzed the Fourier components of broken end ring segments and compared them with those of the broken bars. We have verified, by both experiment and simulation, that the components of $(1 \pm 2s)f$ of the broken end ring segments are larger than those of the broken bars when the number of faults is one or two. The electromagnetic field in the motor with two broken bars and a broken end ring has been analyzed. Moreover, the effect of the number of broken bars and broken end ring segments on the motor performance has been clarified. The discrete wavelet analysis has shown that there are slight differences in the detail signals in high frequency bands between healthy rotor and the rotor with two broken bars.

Author details

Takeo Ishikawa

Address all correspondence to: ishi@el.gunma-u.ac.jp

Division of Electronics and Informatics, Faculty of Science and Technology, Gunma University, Japan

References

[1] A. H. Bonnett and G. C. Soukup, "Rotor Failures in Squirrel Cage Induction Motors," IEEE Transactions on Industry Applications, vol. IA-22, no. 6, pp. 1165–1173 (1986)

[2] W. T. Thomson and M. Fenger, "Current Signature Analysis to Detect Induction Motor Faults," IEEE Industry Applications Magazine, June/July, pp. 26–34 (2001)

[3] A. Daviu, R. Guasp, J. Folch, and M. Palomares, "Validation of a New Method for the Diagnosis of Rotor Bar Failures via Wavelet Transform in Industrial Induction Machines," IEEE Transactions on Industry Applications, vol. 42, no. 4, pp. 990–996, July–Aug (2006)

[4] O. Moreno, R. Troncoso, V. Frias, R. Gillen, and G. Perez, "Automatic Online Diagnosis Algorithm for Broken-Bar Detection on Induction Motors Based on Discrete Wavelet Transform for FPGA Implementation," IEEE Transactions on Industrial Electronics, vol. 55, no. 5, pp. 2193–2202, May (2008)

[5] R. Guasp, A. Daviu, P. Sanchez, P. Panadero, and P. Cruz, "A General Approach for the Transient Detection of Slip-Dependent Fault Components Based on the Discrete Wavelet Transform," IEEE Transactions on Industrial Electronics, vol. 55, no. 12, pp. 4167–4180, Dec. (2008)

[6] S. H. Kia, H. Henao, and G. A. Capolino, "Diagnosis of Broken-Bar Fault in Induction Machines Using Discrete Wavelet Transform without Slip Estimation," IEEE Transactions on Industry Applications, vol. 45, no. 4, pp. 1395–1404 (2009)

[7] Y. Gritli, C. Rossi, L. Zarri, F. Filippetti, A. Chatti, D. Casadei, and A. Stefani, "Advanced Diagnosis of Broken Bar Fault in Induction Machines by Using Discrete Wavelet Transform under Time-Varying Condition," 2011 IEEE International Electric Machines & Drives Conference (IEMDC), pp. 424–429, 15–18 May (2011)

[8] A. Bouzida, O. Touhami, R. Ibtiouen, A. Belouchrani, M. Fadel, and A. Rezzoug, "Fault Diagnosis in Industrial Induction Machines Through Discrete Wavelet Transform," IEEE Transactions on Industrial Electronics, vol. 58, no. 9, pp. 4385–4395 (2011)

[9] O. A. Mohammed, N. Y. Abed, and S. Ganu, "Modelling and Characterization of Induction Motor Internal Faults Using Finite-Element and Discrete," IEEE Transaction on Magnetics, vol. 42, no. 10, pp. 3434–3436 (2006)

[10] L. Weili, X. Ying, S. Jiafeng, and L. Yingli, "Finite-Element Analysis of Field Distribution and Characteristic Performance of Squirrel-Cage Induction Motor with Broken Bars," IEEE Transaction on Magnetics, vol. 43, no. 4, pp. 1537–1540 (2007)

[11] J. Faiz and B. M. Ebrahimi, "A New Pattern for Detecting Broken Rotor Bars in Induction Motors During Start-Up," IEEE Transaction on Magnetics, vol. 44, no. 12, pp. 4673–4683 (2008)

[12] T. Ishikawa, R. Ishigame, M. Matsunami, and N. Kurita, "Analysis and Failure Diagnosis of Squirrel-Cage Induction Motor with Broken Rotor," Proceedings of the 15th International Conference of Electrical Machines and Systems (ICEMS2012), DS2G2-9, Sapporo (2012)

[13] T. Ishikawa, S. Shinagawa, and N. Kurita, "Analysis and Failure Diagnosis of Squirrel-Cage Induction Motor with Broken Rotor Bars and End Rings," IEEE Journal of Industry Applications, vol. 2, no. 6, pp. 292–297 (2013)

[14] T. Ishikawa, Y. Seki, N. Kurita, and T. Matsuura, "Failure Diagnosis of Brushless DC Motor with Rotor Magnet Defect," IEEE 2011 International Electric Machines and Drives, pp. 1561–1565 (2011)

[15] T. Ishikawa, K. Kurihara, K. Shinohara, and Y. Sato, "Rotor Fault Diagnosis Techniques for Induction Machines," The 2007 Annual Meeting Record IEE Japan IA, 3-S4-3, pp. 9–14 (2007) (in Japanese)